Available online at www.sciencedirect.com

ScienceDirect

Energy Procedia 137 (2017) 366–381

Energy Procedia

www.elsevier.com/locate/procedia

14th Deep Sea Offshore Wind R&D Conference, EERA DeepWind'2017, 18-20 January 2017, Trondheim, Norway

Experimental validation of a time-domain approach for determining sectional loads in a floating wind turbine hull subjected to moderate waves

Chenyu Luan[a,b,c,*], Valentin Chabaud[d], Erin E. Bachynski[b,c,d], Zhen Gao[b,c,d], Torgeir Moan[a,b,c,d]

a Norwegian Research Centre for Offshore Wind Technology, Norway
b Centre for Ships and Ocean Structures, NTNU, Otto Nielsens veg 10, Trondheim, Norway, NO-7491
c Centre for Autonomous Marine Operations and System, NTNU, Otto Nielsens veg 10, Trondheim, Norway, NO-7491
d Department of Marine Technology, Norwegian university of science and technology (NTNU), Otto Nielsens veg 10, Trondheim, Norway, NO-7491

Abstract

To achieve cost-effective and reliable structural design of floating wind turbines, efficient and accurate time domain numerical approaches are required to analyse structural responses in design conditions, e.g. wind and waves. This paper focuses on validation of a time-domain numerical approach for determining forces and moments in structural components of floaters. The approach considers floating wind turbines as a system of several structural components, e.g. blades, rotational shaft, nacelle, tower, mooring lines, columns, pontoons and braces. A finite element model is developed to represent global stiffness of the structural components. The external and inertia loads on the structural components are modelled as distributed loads. Hydrodynamic loads on each structural component are derived from the corresponding hydrodynamic coefficients obtained by solving the first order boundary value problem using WAMIT. A 1:30 scaled braceless semi-submersible model test which implements the ReaTHM® testing approach was done by SINTEF Ocean, formerly MARINTEK, in its ocean basin. Measurements of the global forces and moments at the base of a side column of the model and rigid-body motions of the model are compared to the corresponding simulations. This paper focuses on responses in moderate waves for which linear hydrodynamic loads are applicable. Differences in the corresponding simulations and measurements are found to be small, while possible reasons, e.g. synchronizations, non-linear effects, and uncertainties in the measurements and simulations, for the differences are analysed. Essential information about the model test, descriptions of the numerical models, calibrations and results and discussions of the validation are given in this paper.

Peer-review under responsibility of SINTEF Energi AS.

Keywords: Semi-submersible wind turbine; Sectional loads; Experimental validation; Numerical simulation; Moderate waves

* Corresponding author. Tel.: +47-73595513
E-mail address: Chenyu.luan@ntnu.no

1876-6102
Peer-review under responsibility of SINTEF Energi AS.
10.1016/j.egypro.2017.10.361

1. Introduction

Innovative floating wind turbine concepts are considered an attractive solution for harvesting offshore wind energy in relatively deep water, e.g. deeper than 80 m. The offshore wind industry is moving from pilot prototype field tests to pilot commercial size floating wind farms while structural optimization for cost reduction is a focus of these pilot projects [1, 2].

In general, a floating wind turbine is composed of a rotor nacelle assembly (RNA), a tower, a hull, and a mooring system. Many concepts, e.g. [3-9], have been proposed. These concepts can be classified as spar [3, 4], TLP [5, 6] and semi-submersible wind turbines [7-9].

Floating wind turbines operate in wind, current and waves which result in dynamic motions around mean offsets and structural responses. Limit states with respect to the motions and structural responses are specified in design standards of floating wind turbines, e.g. DNV-OS-J103, ABS #195 and ClassNK guideline [10-12], to make sure that the developed designs will have acceptable stability and structural strength. Consequently, designers must implement appropriate approaches, e.g. numerical simulations and/or model tests, to demonstrate that the designs satisfy the specified requirements and criteria.

Frequency-domain computer codes, e.g. WADAM [25], are widely used in the offshore oil and gas industry to efficiently analyse wave induced rigid-body motions and hydro-pressure forces on mean wetted body surface of a floating unit. The hydro-pressure forces can be used in a finite element analysis [25] to efficiently determine structural responses such as stresses, etc. If the unit has a hull, which is a statically determinate structure, global forces and moments in the hull can be obtained by integrating external and inertia loads which are acting on the corresponding structural components of the hull. Meanwhile, frequency-domain computer codes, e.g. Turbu Offshore [30], are capable of efficient optimizations for designs of offshore bottom-fixed wind turbines. However, validity of the linearized approximations used in the frequency-domain codes must be appropriately checked, in particular for novel designs of floating wind turbines. While we still need to use time-domain simulations and model tests to shed more light on the aero-hydro-servo-elastic feature [13]. Another limitation is that frequency-domain models cannot be used to account for transient loading events, e.g. wind turbine faults. Kvittem and Moan [31] studied a frequency-domain method for estimating short-term tower base bending moments and tower fatigue damage of a semi-submersible wind turbine. In the frequency-domain method, responses to combined wind and wave loads are obtained by superposing responses to separated wind and wave loads. The frequency-domain method was used in a case study to predict bending moments and fatigue damage in tower base of a reference semi-submersible wind turbine in combined wind and wave loads. Predicted results given by carrying out a fully coupled, nonlinear time-domain analysis are considered as reference values. Comparing to the reference values, the fatigue damage predicted by the frequency-domain method were underestimated by 0-60%, corresponding to discrepancies in standard deviations of stress in the order of 0–20%.

Conventional time-domain computer codes [14] focus on simulating global responses of the RNA, tower, and mooring system, and rigid-body motions of floating wind turbines. Finite element models for floating wind turbines are generated and solved in these computer codes. A review of conventional approaches for modelling aerodynamic loads on the RNA and tower and hydro loads on the hull and mooring lines is available in [15]. Morison formula and/or the conventional hybrid frequency-time domain approach [16] are used to model hydro loads on the floating wind turbine's hull. The hull is modelled as a rigid-body with 6 d.o.f.s in the time-domain finite element model, while the conventional hybrid frequency-time domain approach gives integrated forces/moments in 6 d.o.f.s rather than distributed forces and moments. Consequently, sectional forces and moments in the hull cannot be captured in a straightforward manner. A straightforward manner means that the sectional forces and moments can be directly obtained from time-domain simulations and used for design check. This is in contrast to the approach for which a global motion response analysis must be carried out first and then the external aero- and hydro- dynamic loads as well as the inertial loads are applied in a structural analysis of the floater for design check.

Luan et al [16] developed an approach for determining forces and moments in floaters. The approach can be easily implemented in various state-of-the-art computer codes for wind turbine analysis, e.g. Simo/Riflex/Aerodyn, OrcaFlex and FAST+CHARM3D, to extend their capabilities to analyse sectional forces and moments in structural components of a generic floater. The sectional forces and moments in the structural components might be used as input to design formulas for structural strength design checks and/or used as boundary conditions in a sub-model finite element analysis. More details with respect to the difference between the developed approach and conventional approaches, as well features and limitations, can be found in [16].

We intend to, step by step, validate the approach of Luan et al [16] by using measurements of a 1:30 model test of a braceless semi-submersible wind turbine [9] which has been tested in the ocean basin of MARINTEK, now SINTEF Ocean.

In this paper, we focus on comparisons of the responses of the semi-submersible wind turbine in moderate waves with less non-linear effects for which frequency-domain commercial computer codes, e.g. WAMIT, WADAM, can be used as a reference model. Wave-induced transfer functions for rigid-body motions and fore-aft and side-to-side bending moments in base of a side column derived from time-domain and frequency-domain simulations and measurements are compared. The developed time-domain model is expected to give the same results as the commercial computer codes, while the time-domain model can be further used to analyze the sectional forces and moments in the hull in combined wind and wave loads in a straightforward manner but the frequency-domain codes cannot.

The "model-the-model" principle, which means to simulate the actual model tests as closely as possible [17, 18], is used. Uncertainties exist in the measurements, e.g. mass matrices, position of centre of gravity of each component and positions of the anchors. Consequently, necessary calibrations with respect to some inputs of the numerical models are carried out. All numerical results are given by the numerical models with calibrated inputs.

Essential information of the model test, i.e. coordinate systems, measured model properties, environmental conditions and post-processing approach for the measurements, is given in section 2. More details with respect to the model test are referred to [19-21]. The developed numerical models are described in section 3. Calibrations are presented in section 4. Analyses and discussions of the results are available in section 5.

2. The floating wind turbine concept and model test

A layout of the experimental model and definitions of the direction of the wind and waves are shown in Figure 1 in a global Earth-fixed coordinate system (O^g-x^g-y^g-z^g). O^g is at the geometrical center of the water plane area when the model is in calm water. Mass properties and dimensions of the semi-submersible wind turbine are described in a body-fixed coordinate system (O^b-x^b-y^b-z^b) The O^b-x^b-y^b-z^b coordinate system is coincident to the global coordinate system when the model is in calm water. Note that all the data and results presented and discussed in this paper are given in full scale and in the corresponding coordinate systems described in this paper. A linear scaling factor of $\lambda = 30$ and the Froude scaling law are used to scale the original data measured from the model test.

The specified dimensions of the semi-submersible hull are tabulated in Table 1 and shown in Figure 2. As shown in Figure 2, a column which includes two flanges is used to connect "Side column 1" to "Pontoon 1". Fore-aft and side-to-side bending moments in a cross section of the column are measured by strain gauges. The geometric centre of the cross section is (41, 0, -27) in the body-fixed coordinate system. The cross section splits the model into two parts. The part which includes the "Side column 1" is denoted as Part A while the rest is denoted as Part B. Measured mass properties are given in Table 2.

The mooring system is composed of three catenary chain mooring lines with lead wires added for weight correction. Distributions of mass and buoyancy of the mooring lines are made according to a design of the mooring system for which each line has two segments from the fairlead to anchor with constant solid circular cross-section. The design parameters are given in Table 3 and 4. According to the Froude scaling law, the scaled value of the Young's modulus of the mooring lines of the experimental model is $6.3 * 10^9$ kN/m^2.

Environmental conditions of the model tests, for which the results are discussed in this paper, are tabulated in Table 5. In addition, some model tests, e.g. the pull-out tests, decay tests and turbulent wind only tests, are used to calibrate the numerical models.

In the tests with the experimental model, wave elevation at Pos1, see Table 6, was measured and denoted as WAVE1 while in the calibration tests (without the experimental model) wave elevations at Pos1, Pos2 and Pos3 were measured and denoted as WAVE1c, WAVE2c and WAVE3c, respectively. Full-scale horizontal locations of the wave probes in the global coordinate system are given in Table 6.

Table 1. Specified dimensions of the semi-submersible hull (Full-scale)

Central column diameter [m]	6.5
Side column diameter [m]	6.5
Pontoon height [m]	6
Pontoon width [m]	9

Central column freeboard [m]	10
Side column freeboard [m]	20
Centre-to-centre (central to side column) [m]	41
Centre-to-edge (central column to pontoon end) [m]	45.5
Operating draft [m]	30
Displacement [tonne]	10,555

Table 2 Measured mass properties of the experimental model. The center of gravity is described in the body-fixed coordinate system with respect to O^b. The moments of inertia are about the center of gravity.

	Mass [tonnes]	Centre of gravity [m]			Moments of inertia [tonnes*m^2]					
		x^b	y^b	z^b	I_{xx}	I_{yy}	I_{zz}	I_{xy}	I_{xz}	I_{yz}
Complete model	9,730	0	0	-19.05	10297582	10297582	7641621	0	0	0
Part A	456.7	41	0	-12.93	96093	96093	2193	0	0	0

Table 3. Design parameters of a single mooring line

Segment	Length (m)	Mass per length (kg/m)	Wet weight (kN/m)	Specified diameter (m)
Upper	240.00	235.0	2.005	0.195
Lower	367.55	446.0	3.804	0.269

Table 4. Arrangement of the mooring line anchors and fairleads described in the global coordinate system

Fairlead	x^g	y^g	z^g	Anchor	x^g	y^g	z^g
1	45.95	0	-27	1	603	0	-200
2	-22.98	39.8	-27	2	-301.5	522.2	-200
3	-22.98	-39.8	-27	3	-301.5	-522.2	-200

Table 5 Environmental conditions of selected model tests

Reference No.	H_s [m]	[s]	Wave direction [degree]	Model test duration [hour]	Note
2310	2	Period range:3.5-22	0	3	Pink noise tests
2321	4	Period range: 4.5-22			
2420	3.6	T_p: 10.2	0	3	JONSWAP spectrum

Table 6 Wave probe position in calibration (in the O^g-x^g-y^g-z^g coordinate system)

	x^g (m)	y^g (m)
Pos1	-187.5	-94.2
Pos2	0	0
Pos3	0	-94.2

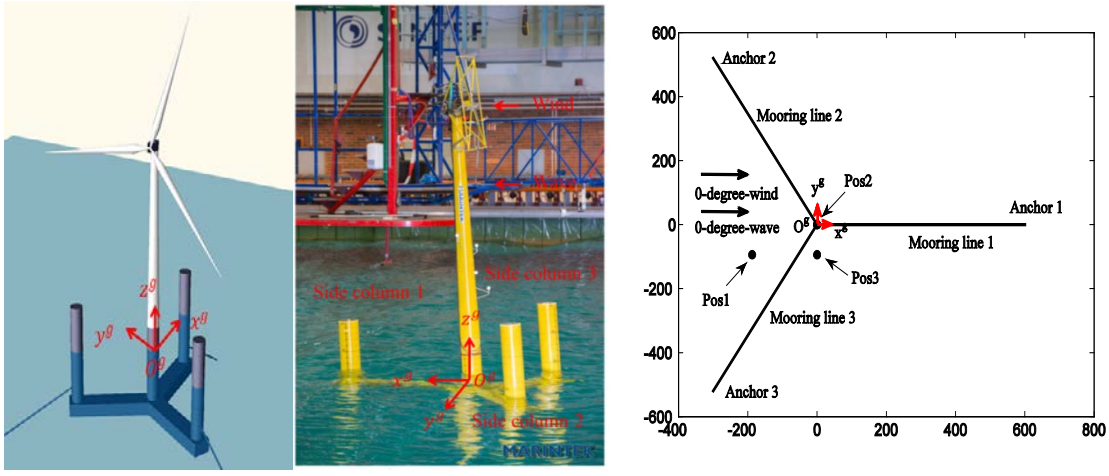

Figure 1 Layout of the experimental model

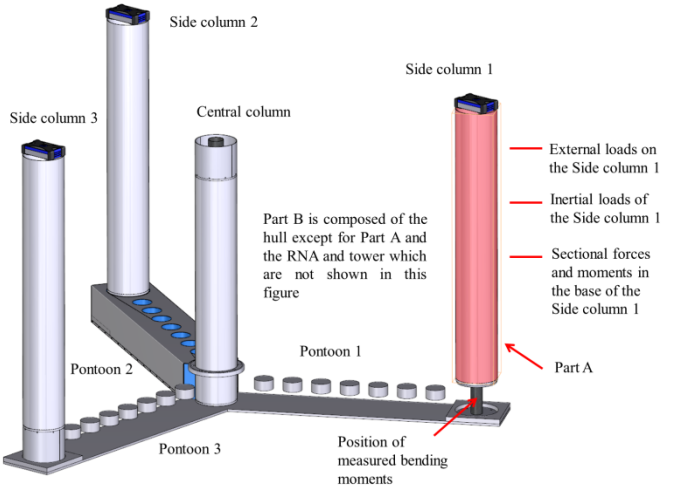

Figure 2 A layout of the hull of the experimental model, courtesy of Fredrik Brun (SINTEF Ocean). Note that the configurations of the three pontoons are identical. Some parts of the configurations of Pontoon 1 and 3 are not shown.

3. Numerical methods and models

A time-domain model (TDM) and a frequency-domain model (FDM) are developed to calculate the forces and moments in the aforementioned cross section for which the geometric center of the cross section is (41, 0, -27) in the O^b-x^b-y^b-z^b coordinate system. The forces and moments are denoted as F_x, F_y, F_z, M_x, M_y, and M_z and described in a body-fixed coordinate system (O^{inp}-x^{inp}-y^{inp}-z^{inp}) with respect to O^{inp}. The O^{inp}-x^{inp}-y^{inp}-z^{inp} and O^b-x^b-y^b-z^b coordinate systems are coincident except that O^{inp} is located at (41, 0, -27) in the O^b-x^b-y^b-z^b coordinate system. M_x and M_y correspond to the side-to-side and fore-aft bending moments, respectively.

3.1. TDM

We denote the Simo/Riflex [43, 44] time-domain finite element model for calculating sectional forces and moments in the cross-section between Parts A and B as TDM.

The finite element model is generated in Riflex in the global coordinate system. The model is composed of 183 truss elements for modelling the three mooring lines, three artificial beam elements for capturing the sectional forces and moments in the cross-section and two control nodes for modelling external and inertial loads on the Parts A and B.

The approach, which is initially described in [16], is used in Simo to calculate the external and inertial loads on Parts A and B. The loads given by Simo are described in the corresponding body-related coordinate systems ($O^{r,A}$-$x^{r,A}$-$y^{r,A}$-$z^{r,A}$ and $O^{r,B}$-$x^{r,B}$-$y^{r,B}$-$z^{r,B}$) respectively and transferred to the control nodes of the finite element model. Each control node has 6 d.o.f.s. Each of the end nodes of the artificial beam elements and the top end nodes of the mooring lines (the fairleads) rigidly follows the motions of the corresponding control node. The O^b-x^b-y^b-z^b and body-related coordinate systems are coincident when the model is located at its mean position in calm water. $O^{r,A}$ and $O^{r,B}$ rigidly follow rigid-body motions of the O^b but the orientation of the body-related coordinate systems and vertical position of the $O^{r,A}$ and $O^{r,B}$ are fixed (as the same as the body-related coordinate systems when the model is located at its initial position in time-domain simulation). To obtain the first order hydro loads, boundary value problem in an earth-fixed coordinate system (e.g. O^g-x^g-y^g-z^g) with assumption that the hull is a rigid-body needs to be solved to derive the corresponding coefficient vectors and matrices. Note that the derived coefficient vectors and matrices include hydrodynamic interactions. Second order and higher order hydrodynamic loads and hydroelastical effects are not included. More details are available in [16].

Morison's formula is used to model the hydrodynamic loads on the mooring lines, while the drag term of the Morison's formula is use to model the drag forces on Parts A and B. A discussion with respect to selection of the corresponding drag coefficients (C_d) and added mass coefficients (C_a) is given in section 4.

Young's modulus of mooring lines of the numerical model is specified as $2.1 * 10^8$ kN/m^2 rather than the value of the experimental test ($6.3 * 10^9$ kN/m^2) to avoid numerical problems. In theory, effects of this difference on mooring line tensions and global responses of the model are negligible.

In Riflex, the time-domain finite element model is solved by using the Newmark-β numerical integration ($\beta = 3.9$ and $\gamma = 0.505$). Time step is set to be 0.05 seconds. Rayleigh damping, which is a linear combination of the Riflex generated global mass and stiffness matrices, is used for modelling effect of structural damping. The corresponding mass and stiffness proportional coefficients are set to be 0 and 0.005, respectively. More explanations are given in [24].

3.2. FDM

WADAM implements a function for which a specified plane, e.g. the y-z plane at x=5, automatically divides the hull into two parts, and calculates sectional forces and moments that are in equilibrium to inertial and external hydro-loads on each part. However, we cannot use this function to calculate the forces and moments in the base of the side column of our model since the specified plane in WADAM is infinite. If we specified an x-y plane at z=-24, one of the parts divided by the specified plane would be composed of the wetted surface of the three side columns and the central column. Consequently, the FDM, which implements the same principle as WADAM for calculating wave induced transfer functions for rigid-body motions and sectional forces and moments but is more flexible for users to divide the wetted surface into user specified parts, is developed in Matlab [22] and validated by using WADAM. Note that the FDM implements linear theory [25]. Viscous drag forces on the hull and hydroelastic effects are not included.

The implemented principle is described as follows:

The transfer functions for the sectional forces and moments ($\boldsymbol{R}^s(\omega)$) can be derived from $\boldsymbol{R}^s(\omega,t) = \mathcal{R}\{\boldsymbol{R}^s(\omega)e^{-i\omega t}\}$. $\boldsymbol{R}^s(\omega,t)$ denotes the global forces and moments induced by a unit-amplitude regular wave for which second order and higher order terms with respect to amplitude of the regular wave are removed. The hull of the experimental model is a statically determinate structure. As a result, the global forces and moments ($\boldsymbol{R}^s(\omega,t)$) are in equilibrium with inertia loads ($\boldsymbol{R}^i(\omega,t)$) and external loads ($\boldsymbol{R}^e(\omega,t)$) on the Part A, see Figure 2 and Eq. (1). $\boldsymbol{R}^i(\omega,t)$ is determined by the mass matrix of Part A and acceleration ($\ddot{\boldsymbol{Y}}(\omega,t)$). $\ddot{\boldsymbol{Y}}(\omega,t)$ is obtained by solving the equations of motion in the the O^g-x^g-y^g-z^g coordinate system, see Eq. (2). Rigid-body motions are denoted as $Y(\omega) = [Y_1, Y_2, Y_3, Y_4, Y_5, Y_6]$. $\boldsymbol{Y}(\omega,t) = \mathcal{R}\{\boldsymbol{Y}(\omega)e^{-i\omega t}\}$ denotes the 6 d.o.f. rigid-body motions induced by a unit-amplitude regular wave. $\mathcal{R}\{\}$ denotes the real part of the complex value inside the bracket. Approaches for generating and solving the equations of motion are well known and referred to [26]. In Eq. (1), $\boldsymbol{M}^g$, $\boldsymbol{A}^g(\omega)$, $\boldsymbol{B}^g(\omega)$, $\boldsymbol{C}^g$and $\boldsymbol{H}^g(\omega)$ are the mass matrix, added mass coefficient matrix, potential damping coefficient matrix, restoring coefficient matrix and first order wave excitation load transfer function. The $\boldsymbol{R}^e(\omega,t)$ is composed of wave excitation loads ($\boldsymbol{R}^{waex}(\omega,t)$), added mass forces ($\boldsymbol{R}^{add}(\omega,t)$), potential damping forces ($\boldsymbol{R}^{pd}(\omega,t)$) and $\boldsymbol{R}^{flu}(\omega,t)$. $\boldsymbol{R}^{waex}(\omega,t)$, $\boldsymbol{R}^{add}(\omega,t)$, and $\boldsymbol{R}^{pd}(\omega,t)$ can be obtained by 1) solving the potential-flow boundary value problem with the assumption that the hull of the model is a rigid-body; 2) calculating the corresponding pressure forces on the mean wetted body surface of the Part A based on the Bernoulli's equation and the corresponding velocity potential, and 3) integrating the pressure forces and transfer the integrated forces and moments to the corresponding coordinate system. $\boldsymbol{R}^{flu}(\omega,t)$ is the resultant forces and moments of gravity, hydrostatic pressure forces on the outer surface and the atmospheric pressure forces on the inner surface of the Part A when the model is located at an instantaneous position. Note that second and higher order terms with respect to amplitude of the regular wave are not included in the $\boldsymbol{R}^i(\omega,t)$ and $\boldsymbol{R}^e(\omega,t)$ as well.

$$\boldsymbol{R}^s(\omega,t) + \boldsymbol{R}^i(\omega,t) + \boldsymbol{R}^e(\omega,t) = 0 \quad (1)$$

$$\mathcal{R}\{\big(\boldsymbol{M}^g + \boldsymbol{A}^g(\omega)\big)\ddot{\boldsymbol{Y}}(\omega,t) + \boldsymbol{B}^g(\omega)\dot{\boldsymbol{Y}}(\omega,t) + \boldsymbol{C}^g\boldsymbol{Y}(\omega,t)\} = \mathcal{R}\{\boldsymbol{H}^g(\omega)e^{-i\omega t}\} \quad (2)$$

4. Calibration of numerical model

The "model-the-model" principle, which means to simulate the actual model tests as closely as possible [18], is used. A rational calibration procedure for the mooring system is available in [27] and implemented in this paper. C_d and C_a for the segments of each mooring line are specified as 1.4 and 1.0 respectively. The anchors of the mooring lines are moved 1.5 meters away along the radial direction to increase the simulated pretension of each mooring line in calm water from 1,517 kN to 1,597 kN. As discussed in [27], the deviation can be attributed to small inaccuracies in the setup of the model test, e.g. the actual positions of anchors deviated from the specified positions and the actual lengths of the mooring lines were slightly shorter than the specified values.

The mass of the experimental model can be estimated based on the draft, configuration of the hull and resultant force of the vertical components of the mooring line tensions at the fairleads. Comparing the estimated mass to the measured mass (which is tabulated in Table 2), a 4.7% deviation is observed. Meanwhile there are discrepancies between the simulated and measured roll/pitch natural periods (obtained from decay tests) and mean heeling angle and fore-aft and side-to-side bending moment in turbulent wind-only conditions. As discussed in [27], deviations may exist in the measurements of the position of the centre of gravity and moment of inertia.

Consequently, a constant force which is acting on the $O^{r,Part\ B}$ and pointed to the negative axis of $z^{r,Part\ B}$ is added in the TDM model to compensate the 4.7% difference and make the numerical model float at the same draft as the experimental model in calm water while the vertical position of the centre of gravity and mass matrix of Part A and B are calibrated.

The centre of gravity of the Part A is adjusted to (41, 0, -15.3) in the body-fixed coordinate system to give the TDM the same mean bending moments as the measurements when the experimental and numerical models are subjected to the same static tilt angle. The centre of gravity of the Part B is adjusted to (-2.019, 0, -20.6) so that the TDM and experimental model have the same title angle under the same overturning moment. Adjustment of the centre of gravity of the Part A has limited effects on the centre of gravity of the whole model. The relative difference between the adjusted and original vertical positions of the centre of gravity of Part B is 6% (compared to [27]).

Three forces and moments are used to adjust the inertial loads of Part B and denoted as $\boldsymbol{M}_{ad}^{B}\ddot{\boldsymbol{\eta}}^{B}(t)$. The $\boldsymbol{M}_{ad}^{B}$ is a 6×6 matrix. The $\ddot{\boldsymbol{\eta}}^{B}(t)$ is the simulated motions of Part B. The $\boldsymbol{M}_{ad}^{B}$, $\ddot{\boldsymbol{\eta}}^{B}(t)$ and $\boldsymbol{M}_{ad}^{B}\ddot{\boldsymbol{\eta}}^{B}(t)$ are described in the $O^{r,B}$-$x^{r,B}$-$y^{r,B}$-$z^{r,B}$ coordinate system with respect to the $O^{r,B}$. According to the results of a parametric study with respect to the effect of each term in the $\boldsymbol{M}_{ad}^{B}$ on the motion responses and bending moments, all the terms in the $\boldsymbol{M}_{ad}^{B}$ are zero except for $m_{11} = m_{22} = 571$ tonnes and $m_{24} = m_{42} = 5690$ tonnes*m^2. Relative differences between the adjusted terms and the corresponding terms in the original measured mass matrix of Part B are less than 6%.

Adjustments with respect to the terms in the mass matrix of the Part A are not considered since a parametric study shows that reasonable variations, e.g. in a range from -10% to 10%, have very limited effects on the motion responses and bending moments.

The non-dimensional drag coefficients (C_d) for the width and height of the pontoons and the columns are specified as 2.1, 1.7 and 0.5, respectively, according to [28]. Results of a sensitivity study show that the effect of the drag coefficients on the simulated global forces and moments and rigid-body motions are negligible in the wave frequency range, i.e. from 0.3 rad/s to 1.4 rad/s.

5. Results and discussions

In this section we intend to compare the simulated and measured responses, i.e. the fore-aft and side-to-side bending moments and rigid-body motions, of the model in moderate wave-only conditions.

5.1. General

WAVE2c are the measurements of undisturbed waves at Pos2 in wave calibration tests (without the experimental model). WAVE2c were synchronized with the measurements of the model tests by comparing the WAVE1 and WAVE1c from the time 0 to 100 seconds (full-scale) since the WAVE1 and WAVE1c were measured by the same wave probe at the same position in the model tests and wave calibration tests, and radiation and diffraction effects of the experimental model on the wave elevations at the Pos1 are expected to be negligible in the first 100 seconds. The synchronized WAVE2c are considered as measurements of incident waves of the corresponding model tests (with

the experimental model) and were used as input to the TDM.

Lowpass Butterworth filter [22] and zero-phase digital filtering are used to remove high frequency components in the measurements. The cutoff frequency, which is the frequency where the magnitude responses of the filter is $\sqrt{1/2}$, is specified as 0.5 Hz. Then, the measurements are downsampled from 111.11 Hz to 5 Hz without risk of aliasing.

Skewness and kurtosis [29] of the measured and simulated responses and waves are around 0 and 3, respectively and indicate that, in moderate waves, the experimental model and TDM are linear systems with respect to waves (input, denoted as x) and the corresponding response (output, denoted as y). Therefore, wave induced transfer function ($H_{xy}(\omega)$), which is composed of the response amplitude operator (RAO) and phase angle (α), are derived by using Eq. (3, 4). G_{xy} and G_{xx} are one-side spectra that are derived from the corresponding cross-correlation and autocorrelation with respect to the realizations of x and y, respectively [29]. $H_{xy}(\omega)$ is a complex number. Real and imaginary parts are denoted as Re and Im respectively. The phase angle (α) is derived based on the corresponding values of Re and $-Im$. A negative phase angle (α) means the y lags the x. Note that computation of the phase angle of the $H_{xy}(\omega)$ derived from measurements of the incident waves and corresponding responses is very sensitive to the synchronization in particular for high-frequency components of the transfer functions. For example, a 0.4 seconds mismatch means a 9-degree-shift and a 32-degree-shift of the phase angle for the wave components for which the frequency is 0.4 rad/s and 1.4 rad/s, respectively.

$$H_{xy}(\omega) = \frac{G_{xy}(\omega)}{G_{xx}(\omega)} = Re + iIm \tag{3}$$

$$\text{RAO} = \sqrt{Re^2 + Im^2} \tag{4}$$

The linear characteristic of the system can also be checked by calculating the corresponding coherence function $\gamma_{xy}^2(\omega)$, see Eq. (5), [29]. The values of γ_{xy}^2 will always satisfy $0 \leq \gamma_{xy}^2 \leq 1$. The γ_{xy}^2 will equal to one for an ideal constant parameter linear system. G_{yy} is one-side spectrum that is derived from the corresponding autocorrelation with respect to the realizations of y.

$$\gamma_{xy}^2(\omega) = \frac{|G_{xy}(\omega)|^2}{G_{xx}(\omega)G_{yy}(\omega)} \tag{5}$$

5.2. Comparisons of transfer functions

Transfer functions are derived from 1-hour measurements of the pink noise and Jonswap spectrum model tests, i.e. model test 2310, 2321 and 2420, and the corresponding simulations. Reasonably good agreement between the RAOs of the experimental and numerical models is observed, see Figure 3-6. In the comparisons, we focus on frequency ranges where majority of the wave energy is distributed (from 0.4 rad/s to 1.4 rad/s for the pink noise model tests and from 0.5 rad/s to 1 rad/s for the Jonswap spectrum model test). Spectral densities of the waves are given in Figure 7. In addition, the work of Bachynski et al [19] shows that the RAOs which are derived from the pink noise and regular wave model tests are consistent.

Peaks at 0.8 and 1.25 rad/s and trough at 1 rad/s are observed in the RAO for the fore-aft bending moment, see Figure 3. The peaks and trough are attributed to inertial loads and added mass forces which are related to second derivatives of surge and pitch motions (accelerations). Two troughs nearby 0.8 and 1.25 rad/s and a peak nearby 1 rad/s can be observed in the RAO for surge motion.

More significant discrepancies are in comparisons of the phase angles of the transfer functions, in particular for frequencies that are higher than 0.9 rad/s. For the fore-aft bending moments in Figure 3, absolute value of the difference between the phase angle given by the FDM and the phase angle given by experimental measurements or simulations is less than 10 degrees at 0.4 rad/s (the frequency), but up to 50 degrees at 1.4 rad/s. For surge, heave and pitch motions, large differences between the phase angle given by the FDM and the phase angle given by experimental measurements or simulations are in frequency ranges where amplitudes of the corresponding RAOs are

very small (close to zero).

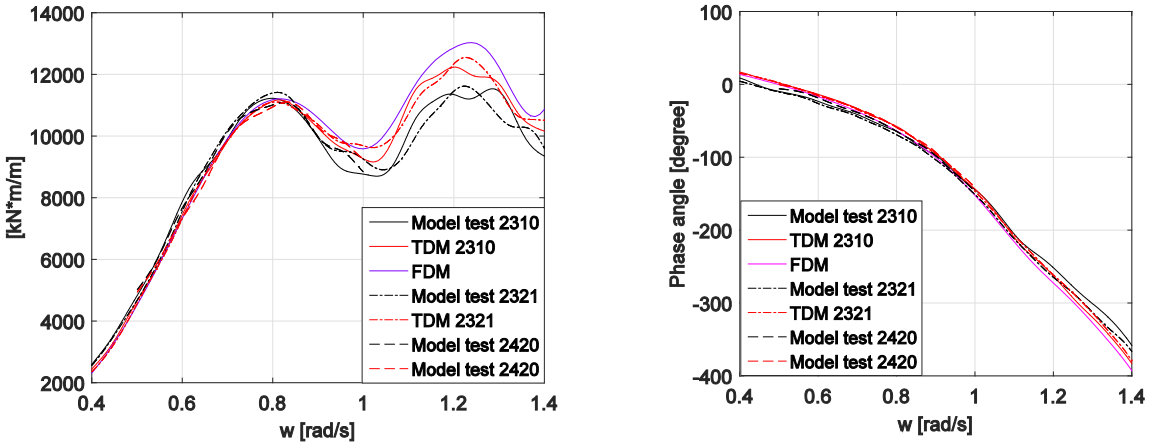

Figure 3 Transfer function for the fore-aft bending moment, derived from 1-hour realizations, pink noise, $H_s = 2$ m (2310) and $H_s = 4$ m (2321), and Jonswap spectrum, $H_s = 3.6$ m and $T_p = 10.2$ seconds (2420)

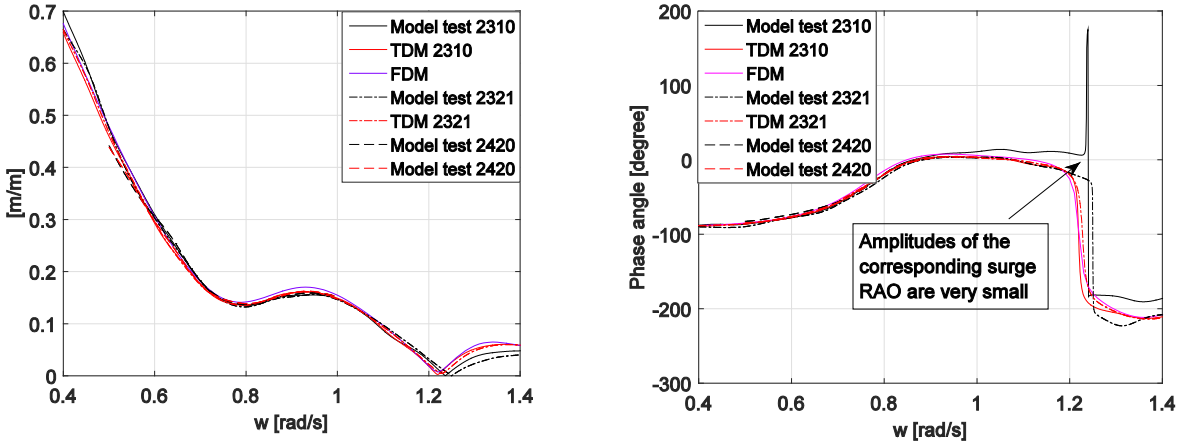

Figure 4 Transfer function for surge, derived from 1-hour realizations, pink noise, $H_s = 2$ m (2310) and $H_s = 4$ m (2321), and Jonswap spectrum, $H_s = 3.6$ m and $T_p = 10.2$ seconds (2420)

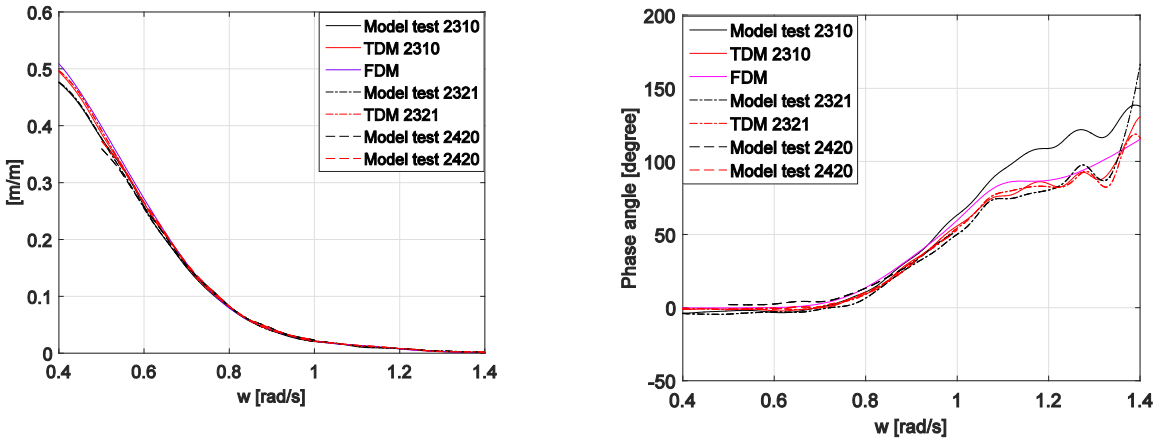

Figure 5 Transfer function for heave, derived from 1-hour realizations, pink noise, $H_s = 2$ m (2310) and $H_s = 4$ m (2321), and Jonswap spectrum, $H_s = 3.6$ m and $T_p = 10.2$ seconds (2420)

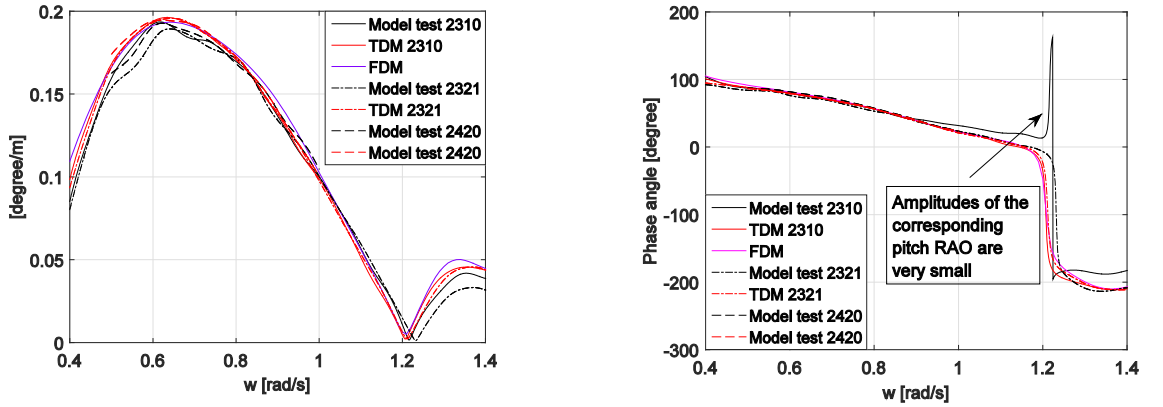

Figure 6 Transfer function for pitch, derived from 1-hour realizations, pink noise, $H_s = 2$ m (2310) and $H_s = 4$ m (2321), and Jonswap spectrum, $H_s = 3.6$ m and $T_p = 10.2$ seconds (2420)

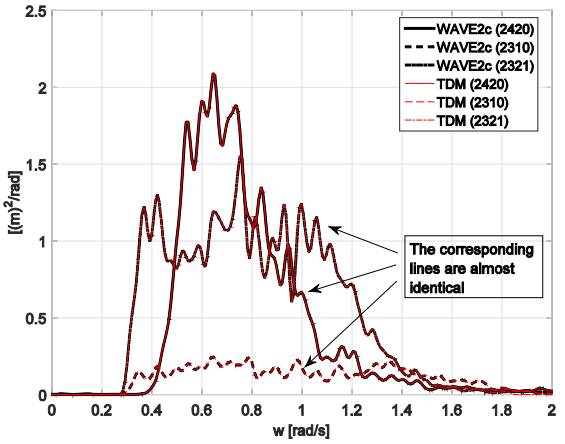

Figure 7 Spectral densities of measured and simulated wave elevations at Pos2 (WAVE2c), derived from 1-hour realizations

5.3. Investigation of differences between simulation and experiment

Some explanations for differences in the transfer functions between the TDM and experimental model are 1) some non-linear effects, e.g. second and higher order hydrodynamic loads and non-linear wave kinematics, which inherently exist in the model tests but are not modelled numerically, and 2) uncertainties, noise and unknown errors in the measurements. Some relevant observations are discussed as follows.

Coherence functions are expected to equal to one when the TDM and experimental model are subject to small incident waves, e.g. the pink noise model test 2310. However, as shown in Figure 8, significant deviations can be observed in the coherence function of the measurements in the frequency range from 1 rad/s to 1.4 rad/s. The deviations indicate that one or more of three possible physical situations exist. The three possible situations are 1) extraneous noise is present in the measurements; 2) the system relating the incident wave (input) and the corresponding response (output) is not linear; and 3) the response is an output due to an input of the wave elevation as well as to other inputs.

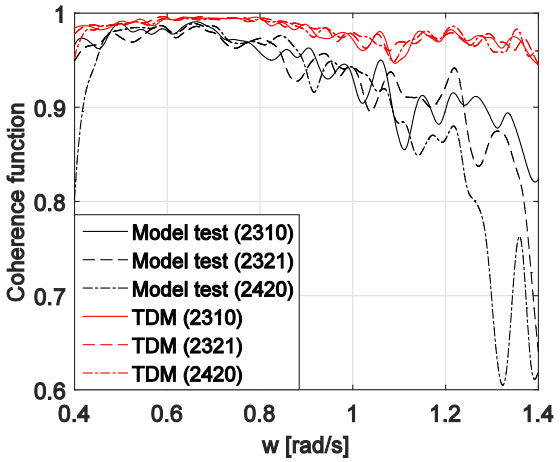

Figure 8 Coherence functions between incident waves (input) and the fore-aft bending moment (output), derived from 1-hour realizations, pink noise, $H_s = 2$ m (2310) and $H_s = 4$ m (2321), and model test 2420, $H_s = 3.6$ m and $T_p = 10.2$ s

Statistical moments, i.e. skewness and kurtosis, are used to analyse characteristics of probability distributions of the measurements with and without implementing a highpass Butterworth filter [22]. The cutoff frequency [22] is 1.2 rad/s. The use of the highpass filter removes the frequency components below 1 rad/s. The results, see Table 7, show that 1) in full frequency range (without filter) the skewness and kurtosis of the measurements are close to 0 and 3, respectively, and indicate that Gaussian distribution can be used to model the probability distribution of the measurements; 2) measurements of the responses are dominated by components that are linearly proportional to the corresponding components of the measured incident waves since in the full frequency range the measured waves and responses can be described by Gaussian distributions; and 3) non-Gaussian components exist in the measurements in particular for the low frequency range due to slow varying drift force on the model and frequency range above 1 rad/s where the corresponding coherence functions significantly deviate from 1. For example, the kurtosis of the measured pitch motion in the model 2321 is 3.68 and 2.99, with and without filter respectively. The kurtosis of the measured wave elevation in the model test 2321 is 3.05 and 6.01, with and without filter respectively.

Some statistical values of the measured and simulated wave elevations are tabulated in Table 8. Airy wave theory is implemented in the TDM. The spectral densities and standard deviations of the simulated and measured wave elevations are almost identical, see Figure 7. However the relevant difference between the maximum values of 1-hour wave elevation of the simulation and measurement can be more than 19% (in the Pink noise model test 2321), also see Figure 9.

Table 7 Skewness and kurtosis of measurements with and without filter

		Measurements	Wave	M_y	Surge	Heave	Pitch
Skewness	2420	Full frequency range	0.09	0.02	-0.10	0.08	0.24
		Above 1 rad/s (after filtering)	0.38	0.00	-0.11	0.96	0.02
	2310	Full frequency range	0.13	0.08	-0.08	0.07	-0.03
		Above 1 rad/s (after filtering)	0.34	-0.02	-0.02	-0.87	0.01
	2321	Full frequency range	0.15	0.04	-0.05	0.03	0.03
		Above 1 rad/s (after filtering)	0.78	0.06	-0.12	2.49	-0.04
Kurtosis	2420	Full frequency range	3.00	3.08	3.05	2.93	3.14
		Above 1 rad/s (after filtering)	3.64	3.14	8.21	56.72	3.06
	2310	Full frequency range	3.17	3.02	2.53	2.97	3.19
		Above 1 rad/s (after filtering)	3.90	3.00	3.14	32.70	3.21
	2321	Full frequency range	3.05	2.99	2.77	2.92	3.68
		Above 1 rad/s (after filtering)	6.01	3.87	5.17	233.01	2.99

Table 8 Statistical values of simulated and measured wave elevations

Unit [m]		2310	2321	2420
Std	Model test	0.47	1.00	0.92
	TDM	0.47	0.99	0.92
Max	Model test	1.89	3.89	4.00
	TDM	1.78	3.15	3.89
Min	Model test	-1.62	-3.08	-3.03
	TDM	-1.63	-3.33	-3.02
Skewness	Model test	0.13	0.15	0.09
	TDM	0.11	0.02	0.10
Kurtosis	Model test	3.17	3.05	3.00
	TDM	3.12	2.92	2.99

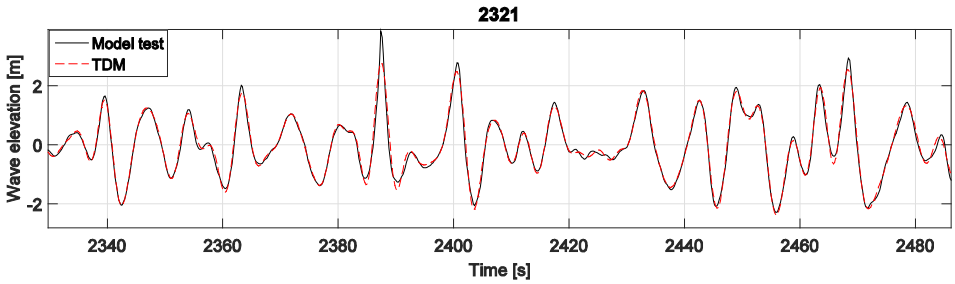

Figure 9 Comparisons of measured and simulated wave elevation realizations. Pink noise model test 2321

Incident wave elevations are measured at the Pos2. However, there is a difference between the mean position of the experimental model, which is induced by mean drift forces on the model, and the Pos2. Fortunately, the difference is negligible since, in moderate wave conditions, the mean offset of the model is relatively small compared to wave length of the incident waves. For instance, the mean offset is less than 0.2 meters (in full-scale) while the wave length of a 4-second-period wave, approximately, is 25 meters.

Transfer functions that are derived from different sets of 1-hour simulations subjected to different moderate waves are more consistent than the transfer functions derived from different sets of 1-hour measurements, see Figure 10 as an example. To quantify uncertainties in the measurements, well designed and systematical repeat-model tests are needed and should be analysed in future.

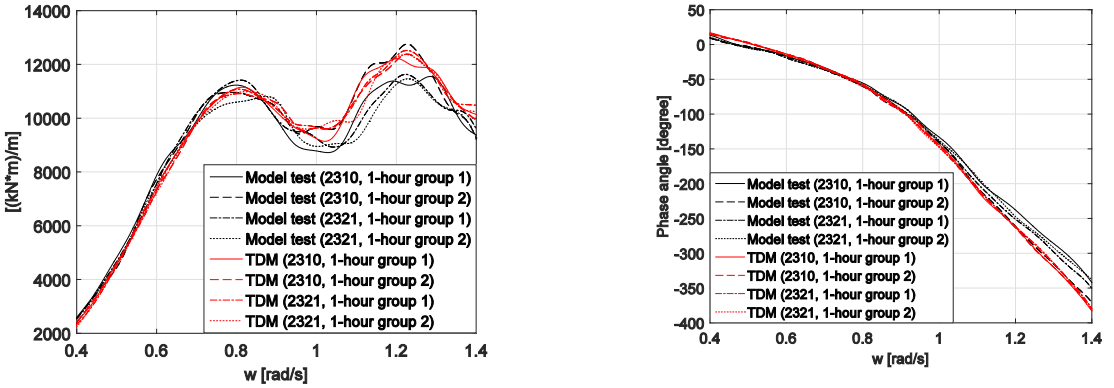

Figure 10 Transfer functions of the fore-aft bending moment, derived two sets of 1-hour realizations

5.4. Simulations and measurements in a moderate Jonswap wave-only condition

Spectral densities and realizations of the simulated and measured responses, i.e. the fore-aft and side-to-side bending moments and rigid-body motions, of the model in a moderate wave-only condition (model test 2420) are compared. The difference in the standard deviation of the simulated and measured fore-aft bending moment is 1.4% and good agreement is seen in the spectrums and realizations, see Figure 11 and 12. In wave frequency range (from 0.4 rad/s to 1.4 rad/s), good agreement is seen in spectrums of measured and simulated rigid-body motions. Motions induced by the slow varying drift force on the experimental model can be observed in the low frequency range in the spectrums of the measurements, while second and higher order hydrodynamic loads, expect for viscous drag forces, are not included in the TDM.

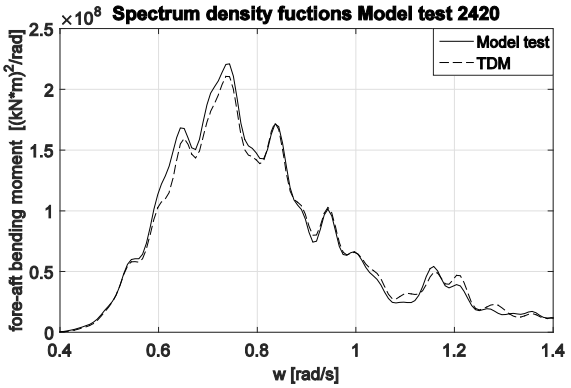

Figure 11 Spectral density functions of the fore-aft bending moment, derived from 1-hour realizations, moderate wave only, $H_s = 3.6$ m and $T_p = 10.2$ s

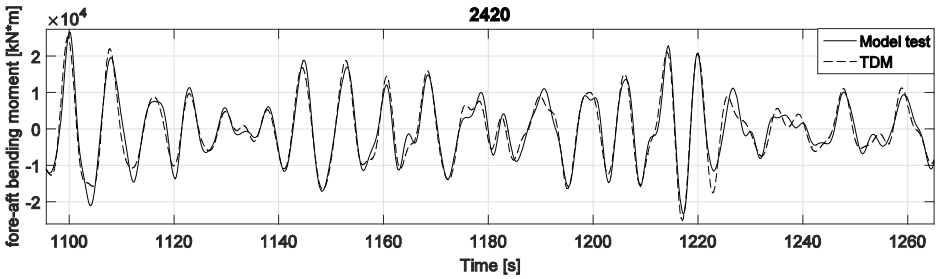

Figure 12 Part of measured and simulated fore-aft bending moment, moderate wave only, $H_s = 3.6$ m and $T_p = 10.2$ s

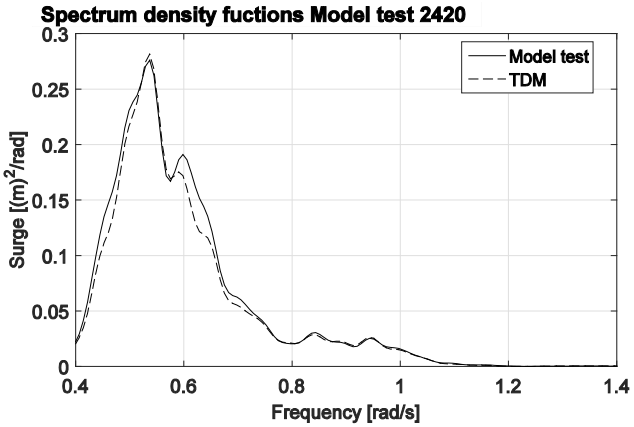

Figure 13 Spectral density functions of surge, derived from 1-hour realizations, moderate wave only, $H_s = 3.6$ m and $T_p = 10.2$ s

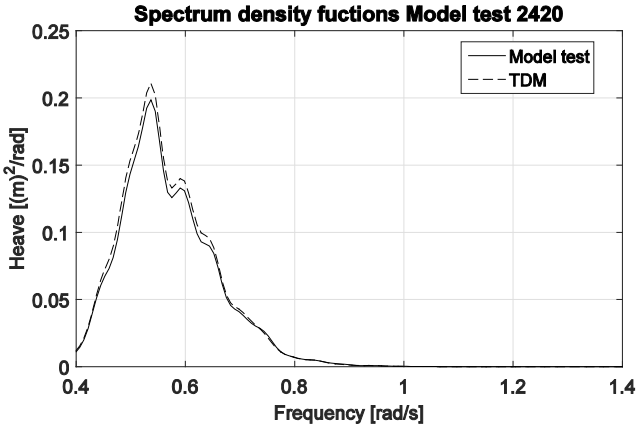

Figure 14 Spectral density functions of heave, derived from 1-hour realizations, moderate wave only, $H_s = 3.6$ m and $T_p = 10.2$ s

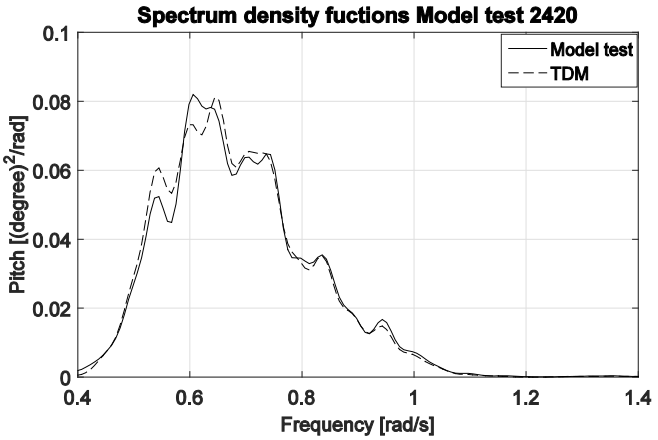

Figure 15 Spectral density functions of pitch, derived from 1-hour realizations, moderate wave only, $H_s = 3.6$ m and $T_p = 10.2$ s

6. Conclusions

Measurements of a 1:30 scaled braceless semi-submersible model test which implements the ReaTHM™ testing approach are used to validate a recently developed time-domain numerical approach for determining forces and moments in floaters. The focus of this paper is on responses in moderate waves. Second order wave loads are expected to be negligible in moderate waves. Statistical values, kurtosis and skewness, for the wave elevations and responses measured in the model test show that the incident waves and corresponding responses are Gaussian-distributed and indicate that the model is linear system with respect to the incident wave (input) and responses (output). Therefore, measurements of the global forces and moments in the base of the side column of the experimental model are compared to the corresponding simulations given by a frequency-domain model (the FDM) and a time-domain model (the TDM). Necessary calibrations with respect to some measured data, i.e. mass matrices, position of centre of gravity and positions of the anchors of the experimental model and drag and added mass coefficients for the hydrodynamic loads on the mooring lines and drag forces on the hull of the model have been carried out according to a rational procedure. The measured wave elevations were synchronized.

Reasonably good agreements are observed in the comparisons between the transfer functions for wave induced rigid-body motions and bending moments at the base of the side column, which are directly given in the FDM and derived from the corresponding simulations and measurements, and comparisons between the corresponding response spectral densities. More differences are observed in comparisons of phase angles of the transfer functions, in particular in frequencies that are higher than 0.9 rad/s. Phase angles of the transfer functions are very sensitive to the synchronizations of the measured data in particular for the higher frequency components of the waves. Due to mean drift forces on the experimental model, there is a difference between the mean position of the experimental model and the Pos2. Fortunately, the difference is negligible in moderate waves. Viscous drag forces have limited effects on the transfer functions. Transfer functions that are derived from different sets of 1-hour simulations subjected to different moderate waves are more consistent than the transfer functions derived from different sets of 1-hour measurements.

The differences in the transfer functions may be arbitrated to 1) some non-linear effects, e.g. second and higher order hydrodynamic loads and non-linear wave kinematics, inherently exist in the model tests but are not modelled numerically; and 2) uncertainties, noise and unknown errors exist in the measurements. Relevant observations in term of coherence functions, statistical properties and realizations are analysed. To quantify the uncertainties in the measurements, well designed and systematical repeat-model tests are needed and should be analysed in future.

Analysis for the comparisons between the simulated realizations and measurements in extreme waves, for which the second-order effects and maybe also high-order effects are critical, will be given in future. Simo/Riflex can account for the second-order wave loads as long as the hull is modelled as one rigid-body. However, to capture the sectional forces and moments in a straightforward manner, the hull needs to be modelled at least as two rigid-bodies. Therefore, additional efforts are needed to develop modelling approaches to address this problem. At the moment, the second-order wave loads are not modelled in the estimation of the cross-sectional loads.

Acknowledgements

The authors acknowledge the financial support provided by the Research Council of Norway through the Centre for Ships and Ocean Structures; the Norwegian Research Centre for Offshore Wind Technology (NOWITECH), NTNU; and the Centre for Autonomous Marine Operations and Systems (AMOS), NTNU.

References

[1] Statoil AS, (2017), http://www.statoil.com/en/TechnologyInnovation/NewEnergy/RenewablePowerProduction/Offshore/HywindScotland/Pages/default.aspx?redirectShortUrl=http%3a%2f%2fwww.statoil.com%2fHywindScotland, accessed 12.January.2017

[2] Principle Power, Inc., (2017), http://www.principlepowerinc.com/, accessed 12.January.2017

[3] Jonkman J., (2010), "Definition of the Floating System for Phase IV of OC3", NREL/TP-500-47535, National Renewable Energy Laboratory, Golden, CO, USA.

[4] Nielsen, F. G., Hanson, T. D., and Skaare, B., (2006), "Integrated Dynamic Analysis of Floating Offshore Wind Turbines," Proceedings of the 25th International Conference on Offshore Mechanics and Arctic Engineering, OMAE2006-92291, Hamburg, Germany.

[5] Bachynski EE, Moan T., (2012), "Design considerations for tension leg platform wind turbines.", Marine Structures, Vol 29, pp 89-114.

[6] Sclavounos, P., Tracy, C., and Lee, S., (2007), "Floating offshore wind turbines: responses in a seastate; Pareto optimal designs and economic assessment", Tech. rep., Department of Mechanical Engineering, Massachusetts Institute of Technology.
[7] Roddier, D., Cermelli, C., Aubault, A., and Weinstein, A., (2010), "WindFloat: A floating foundation for offshore wind turbines", Journal of Renewable and Sustainable Energy 2, 033104, doi:10.1063/1.3435339.
[8] Robertson, A., Jonkman, J., Masciola, M., Song, H., Goupee, A., Coulling, A., and Luan C., (2012), "Definition of the Semisubmersible Floating System for Phase II of OC4", Offshore Code Comparison Collaboration Continuation (OC4) for IEA Task 30.
[9] Luan, C., Gao, Z., and Moan, T., (2016). "Design and analysis of a braceless steel 5-mw semi-submersible wind turbine". Proceedings of the 35th International Conference on Ocean, Offshore and Arctic Engineering, OMAE2016-54848, Busan, Korea, June 19–24.
[10] DNV, (2013), "Offshore standard – Design of Floating Wind turbine Structures", DNV-OS-J103, Det Norske Veritas.
[11] ABS, (2013), "Guide for Building and Classing Floating Offshore Wind Turbine Installations", American Bureau of Shipping.
[12] ClassNK, (2012), "Guidelines for Offshore Floating Wind Turbine Structures", Nippon Kaiji Kyokai.
[13] Cordle, A., and Jonkman, J., (2011), "State of the art in floating wind turbine design tools", Proceedings of the 21st International Offshore and Polar Engineering Conference, Maui, Hawaii, USA. Vol. 1, pp. 367–374.
[14] Robertson, A., Jonkman, J. Qvist, J.,Chen, X., Armendariz,J.A., Soares, C.G., Luan, C., Huang, Y., Yde, A.,Larsen, T., Nichols, J., Lei, Liu, Maus, K.J., Godreau, C., Heege, A., Vatne, S.R., Manolas,D., Qin, H., Riber, H., Abele, R., Yamaguchi, A., Pham,A. Alves,M., Kofoed-Hansen,H., (2014), " Offshore code comparison collaboration, continued: phase II results of a floating semisubmersible wind system", In Proceedings of the 33rd International Conference on Ocean, Offshore and Arctic Engineering, no. OMAE2014-24040, San Francisco, USA, 2014.
[15] Matha, D., Schlipf, M., Cordle, A., Pereira, R., and Jonkman, J., (2011). "Challenges in Simulation of Aerodynamics, Hydrodynamics, and Mooring-Line Dynamics of Floating Offshore Wind Turbines," Proceedings of the 21st International Offshore and Polar Engineering Conference, Maui, Hawaii, USA, Vol. 1, pp. 421–428.
[16] Luan, C., Gao, Z. and Moan, T., (2017), "Development and verification of a time-domain approach for determining forces and moments in structural components of floaters with an application to floating wind turbines". Marine Structures. vol. 5 pp 87-109.
[17] Aksnes, V., Berthelsen, P. A., and Da Fonseca, N. M. M. D., (2015). "On the need for calibration of numerical models of large floating units against experimental data". In Proceedings of 25th Int Offshore and Polar Eng Conf, ISOPE-2015, Kola, Hawaii, USA, June 21–26.
[18] Ormberg, H., Baarholm, R., and Stansberg, C.T., (2003). "Time-domain coupled analysis of deepwater TLP, and verification against model tests". Proc. 13th ISOPE Conf., Honolulu, Hawaii, USA.
[19]Bachynski, E. E., Thys, M., Chabaud, V., and Sauder, T., (2016). "Realtime Hybrid Model Testing of a Braceless Semi-submersible Wind turbine. Part II: Experimental Results". In 35th International Conference on Ocean, Offshore and Arctic Engineering, no OMAE2016-54437.
[20]Sauder, T., Chabaud, V., Thys, M., Bachynski, E. E., and Sæther, L. O., (2016). "Real-time hybrid model testing of a braceless semi-submersible wind turbine: Part I: The hybrid approach". In 35th International Conference on Ocean, Offshore and Arctic Engineering, no. OMAE2016-54435.
[21] Chabaud, V., (2016), "*Real-Time Hybrid Model Testing of Floating Wind Turbines*". Ph.d thesis, ISBN 978-82-326-2083-8., NTNU, Norway.
[22] MathWorks, Inc., (2010), MATLAB: The Language of Technical Computing. Natick, MA: MathWorks.
[23] MARINTEK, (2011). SIMO User's Manual.
[24] MARINTEK, (2013). RIFLEX User's Manual.
[25] DNV, (2013), SESAM User Manual HydroD, Det Norske Veritas.
[26] Faltinsen, O.M., (1990), "*Sea loads on ships and offshore structures*", Cambridge University Press, UK.
[27] Berthelsen, P. A., Bachynski, E. E., Karimirad, M., and Thys, M., (2016). "Real-time hybrid model testing of a braceless semi-submersible wind turbine. Part III: Calibration of a numerical model". In 35th International Conference on Ocean, Offshore and Arctic Engineering, no. OMAE2016-54640.
[28] DNV, (2010), "Recommended Practice - Environmental Conditions and Environmental Loads", DNV-RP-C205, Det Norske Veritas.
[29] Bendat, J. S., and Piersol, A. G., (2010). "*Random Data: Analysis and Measurement Procedures, 4th Edition*". John Wiley & Sons, Inc. ISBN: 978-0-470-24877-5, page 180.
[30] van Engelen, T.G., and Braam, H., (2004). "TURBU Offshore, Computer Program for Frequency Domain Analysis of Horizontal Axis Offshore Wind Turbines; Implementation", ECN-C--04-079, Dutch Ministry of Economic Affairs, Netherlands.
[31] Kvittem, M. I., and Moan, T.,(2015), "Frequency versus time domain fatigue analysis of a semi-submersible wind turbine tower", Journal of Offshore Mechanics and Arctic Engineering, 137(1):011901.